Supporting Information for Fabrication of $Gd_xFe_yO_z$ films using an atomic layer deposition-type approach

Pengmei Yu,† Sebastian M. J. Beer,‡ Anjana Devi,‡ and Mariona Coll*,†

†*Institut de Ciència de Materials de Barcelona (ICMAB-CSIC), Campus de la UAB, 08193 Bellaterra, Barcelona, Spain*

‡*Inorganic Materials Chemistry, Ruhr University Bochum, Universitätsstraße 150, Bochum 44801, Germany*

E-mail: mcoll@icmab.es

Phone: +34 935801853

Fe precursors for ALD

The deposition of iron oxide by ALD has seen a rich variety of precursors explored, *viz.* β-diketonates, alkoxide, halides, metallocenes, amidinate, ketoiminate, etc. as tabulated in Table S1. Among these precursors ferrocene ([$Fe(Cp)_2$]) has been intensively studied due to its commercial availability and low cost. However, despite the fact that its high stability enables safe handling in ambient conditions, ALD iron oxide from [$Fe(Cp)_2$] requires relatively high temperature with molecular O_2[1,2] (> 350 °C) or a strong oxidant like O_3. Nonetheless, the deposition with ferrocene has been reported challenging. For instance, Klahr *et al.*[3] observed a decreased GPC after the first few hundred of cycles, which was believed to be caused by the self-catalytic decomposition of [$Fe(Cp)_2$]. Linear deposition rate was

demonstrated to be achieved by introducing TiO_2 co-deposition.[4] In addition, Avila *et al.* once described [$Fe(Cp)_2$] condensation in the pump and generation of pump malfunction.[5]

Table S1: Fe_2O_3 precursors tested in atomic layer deposition process

Fe precursor	Oxygen source	Deposition temperature	GPC (Å/cycle)	Impurity	Ref
$Fe(acac)_3$	O_2	RT-150	-	-	6
$Fe(thd)_3$	O_3	186	0.11	-	7
$Fe(thd)_3$*	O_3	138-380	0.1-1	-	8
$Fe_2(O^tbu)_6$*	H_2O	130-170	0.26±0.04	-	9
$Fe_2(O^tbu)_6$*	H_2O	180	0.62	-	10
$FeCl_3$	H_2O	500	0.2	-	11
$FeCl_3$	H_2O	200-350	0.6	Cl	12
$FeCl_3$	H_2O	210-360	0.65	Cl	13
$Fe(Cp)_2$	O_2	350-500	1.4	C	1
$Fe(Cp)_2$	O_2	367-534	0.15	-	2
$Fe(Cp)_2$	O_3/O_2 mixture	200	0.2	-	14
$Fe(Cp)_2$	O_3	200	0.62	-	3
$Fe(Cp)_2$	O_3	170-350	1.4	H	15
$Fe(Cp)_2$	O_3	200-325	0.4-0.5	-	4
$Fe(2,4-C_7H_{11})_2$*	H_2O_2	60-120	0.4-0.6	-	16
$Fe(2,4-C_7H_{11})_2$*	O_2	60-120	0.2-0.3	-	16
$Fe(2,4-C_7H_{11})_2$*	O_3	60-120	0.5-0.9	-	16
$Fe(hfa)_2TMEDA$*	O_3	150-350	<0.2	C,H	17
FeAMD	H_2O	130-200	0.55±0.05	-	5
$Fe(^ipki)_2$*	H_2O	100-275	0.47-1.1	C	18

* synthesized
acac = acetylacetonate
$2,4-C_7H_{11}$=2,4−methylpentadienyl
hfa = 1,1,1,5,5,5-hexafluoro-2,4-pentanedionate, TMEDA = N,N,N′,N′-tetramethylethylenediamine
^{i}pki = N-isopropyl ketoiminate

Gd precursors for ALD

In Table S2, the precursors adopted for the ALD Gd_2O_3 synthesis are summarised. β-diketonate $Gd(thd)_3$ and cyclopentadienyl $Gd(^iPrCp)_3$ precursors were mainly used for ALD Gd_2O_3, however the films were mostly reported to be contaminated. Other studies performed combining water and Gd cyclopentadienyl $Gd(CpCH_3)_3$, alkoxide $Gd(mmp)_3$, silylamide $Gd[N(SiMe_3)_2]_3$, where either non-saturative ALD growth or carbon/hydrogen

contamination were observed.[19] ALD Gd_2O_3 process was observed to be self-limiting from another alkoxide $Gd(DMB)_3$ with water, nonetheless the films were also found with carbon and hydrogen impurities. Milanov *et al.*[20] demonstrated an alternative Gd guanidinate [[$Gd(DPDMG)_3$]] (employed in the current study) with considerable thermal stability and optimal reactivity toward H_2O to facilitate higher growth rates, leading to well-defined Gd_2O_3 deposition behaviour.

Table S2: Gd- precursors tested in atomic layer deposition process

Gd precursor	Oxygen source	Deposition temperature (°C)	GPC (Å/cycle)	Impurity	Ref
$Gd[N(Si(Me)_3)_2]_3$	H_2O	150-300	0.6-2.4	-	[21]
$Gd(thd)_3$*	O_3	300	0.3	C,F,H	[22]
$Gd(thd)_3$*	O_3	225-400	0.3	C,H	[23]
$Gd(MeCp)_3$	H_2O	150-350	0.75-2.5	H	[23]
$Gd(mmp)_3$*	H_2O	200-300	0.1-1	-	[24]
$Gd(DMB)_3$*	H_2O	300-400	0.3-0.5	C,H	[25]
$Gd(DPDMG)_3$*	H_2O	160-300	1.1	-	[20]
$Gd(^iPrCp)_3$	O_2 plasma	150-350	1-3.5	-	[26]
$Gd(^iPrCp)_3$	H_2O	300	0.5-2	H	[27]
$Gd(^iPrCp)_3$	O_3	250	0.1-0.4	C	[28]
$Gd(^iPrCp)_2(^iPr{-}amd)$*	H_2O	200-325	0.7-1.7	C,H	[29]
$Gd(^iPrCp)_2(^iPr{-}amd)$*	O_3	200-350	0.4-1.3	C	[29]

* synthesized
thd = 2,2,6,6-tetramethylheptane-3,5-dione
mmp = $OCMe_2CH_2OMe$
DMB = $OC(CH_3)_2CH(CH_3)_2)$
DPDMG = $(^iPrN)_2CNMe_2$
amd = Amidinate

ALD valving systems

In Figure S1 it is shown a scheme of the ALD reactor that is employed in this study. Three different valving systems, that are here identified as flow mode (F), pressure-boost (PB) and exposure mode (E), could be achieved by manipulating the exit valve and ALD valves highlighted in the picture. In F mode a continuous flow of inert gas carries the precursor to the reaction chamber. For low-vapor pressure precursors, PB mode is used with an

elevated vapor pressure before precursor pulses. E mode was applied to enable sufficient surface reaction and deposition homogeneity. In this case, the gas exit valve was closed after precursor dosing. These three modes are explained in more detail in the Experimental part of the main manuscript.

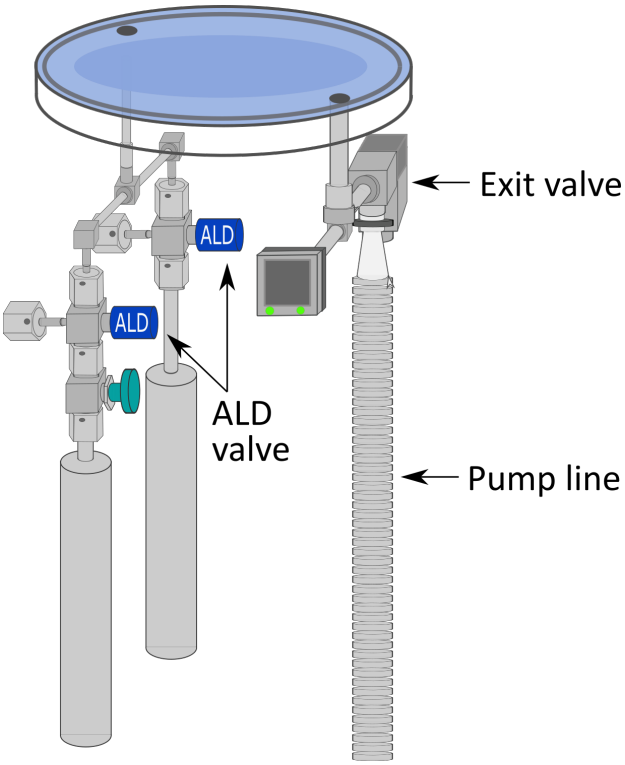

Figure S1: Illustration of the valving system of the ALD reactor: different modes (specifically, flow mode, pressure-boost or exposure mode) can be realised by manipulating the valve opening and closure. (Adapted from Savannah 100 user manual.[30])

Gd_2O_3 films from [Gd(DPDMG)$_3$]

The optimization parameters for gadolinium oxide deposition using an ALD-type approach are displayed in Figure S2(a) heating Gd(DPDMG)$_3$ at $T_{Gd\text{-}subl}$=135 °C under pressure-boost (PB)/flow (F) mode at 160 - 250 °C deposition temperature. Upper panel (blue) identifies depositions investigated using H_2O as co-reactant. Lower panel identifies those tested using

ozone as oxidant. EDX spectrum from the sample prepared in pressure-boost with ozone at 250 °C is shown in Figure S2(b).

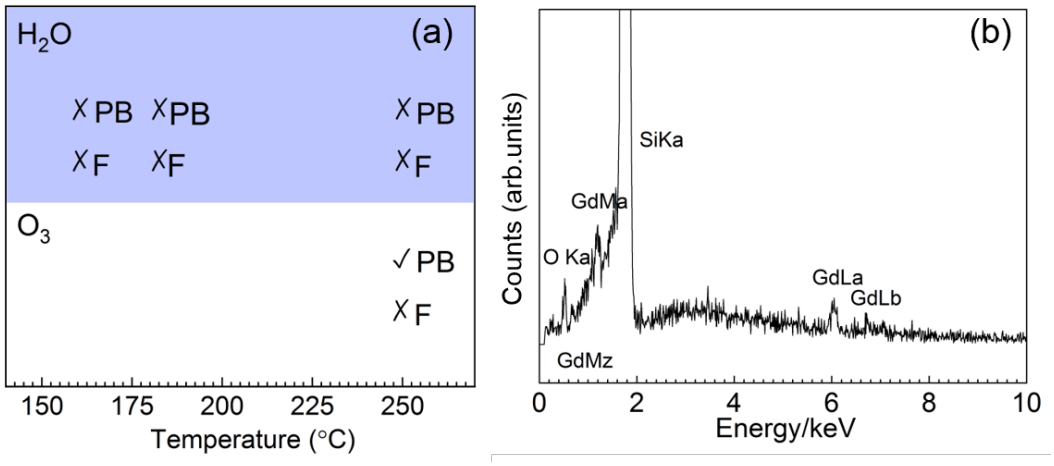

Figure S2: (a) Optimization of Gd_2O_3 deposition temperature from [Gd(DPDMG)$_3$] and O_3/H_2O at sublimation temperature of 135 °C using pressure-boost (PB)/flow (F) mode. (✗: no Gd detection; ✓: Gd detection). (b) EDX spectra from as-deposited sample from [Gd(DPDMG)$_3$] and O_3 at the deposition temperature of 250 °C.

The element concentrations, ratio and film thicknesses obtained from RBS studies for the optimized samples in this work are listed in Table S3.

Table S3: Summary of composition and thickness for Gd_2O_3, Fe_2O_3, Gd-Fe-O ([Fe(Cp)$_2$]+[Gd(DPDMG)$_3$]) and Gd-Fe-O ([Fe(^{i}pki)$_2$]+[Gd(DPDMG)$_3$]) samples from RBS/NRA study. The error margin for C, N and O is approximately 3 at.%

Sample	C (at.%)	N (at.%)	O (at.%)	Fe (at.%)	Gd (at.%)	Metal/O	Fe/Gd	Thickness (nm)
Gd_2O_3	3.3	0.4	73.8	0.2	22.3	0.30	-	80
Fe_2O_3	0.8	0.3	65.0	33.8	0.0	0.52	-	60
Gd-Fe-O ([Fe(Cp)$_2$]+[Gd(DPDMG)$_3$])	1.4	1.0	67.6	17.6	12.4	0.44	1.41	30
Gd-Fe-O ([Fe(^{i}pki)$_2$]+[Gd(DPDMG)$_3$])	0.9	0.2	63.2	17.5	18.2	0.5	0.96	120

Figure S3 shows typical XRR pattern of Gd_2O_3 films that allowed to build the thickness map in the main manuscript (Figure 2).

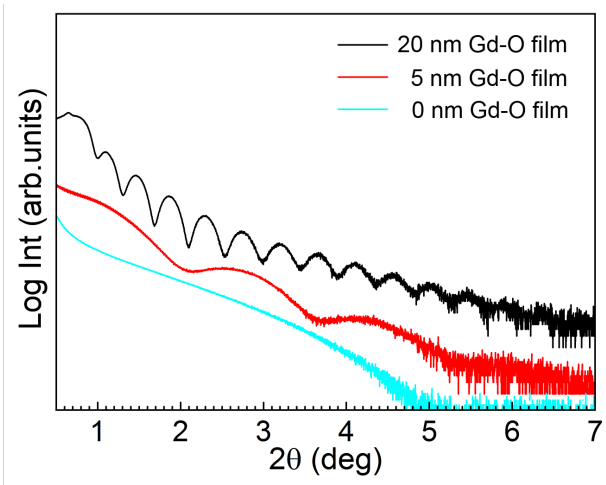

Figure S3: XRR curves of Gd_2O_3/Si samples located at different chamber positions. 40 sccm gas flow.

Fe_2O_3 films from $[Fe(Cp)_2]$

The deposition of Fe_2O_3 using $[Fe(Cp)_2]$ was studied in the 150 - 250 °C temperature window in flow mode (70 sccm) repeating 2000 cycles. Fe was only detected when ozone was used as co-reactant for a temperature range of 200 - 250 °C, see Figure S4(a). Typical EDX analysis from an as-deposited film is shown in Figure S4(b).

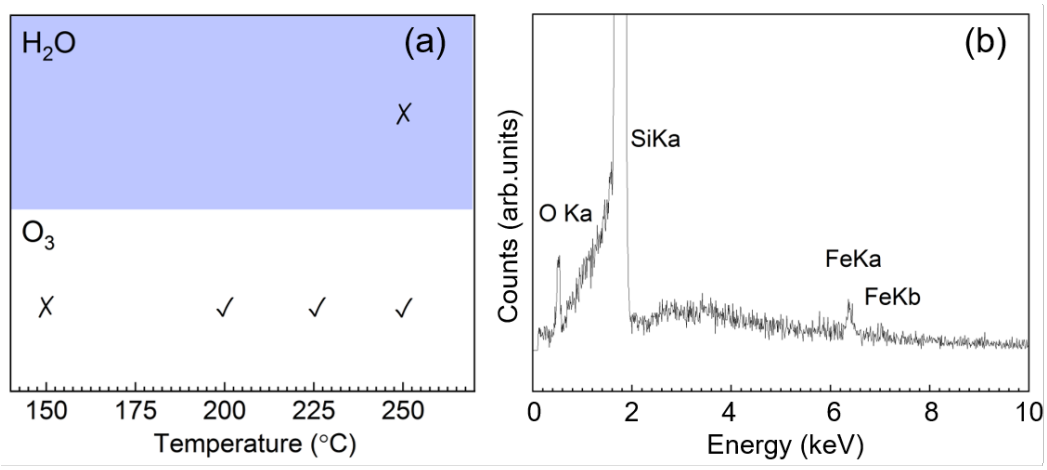

Figure S4: (a) Optimization of Fe_2O_3 deposition from $[Fe(Cp)_2]$ and ozone/water using flow mode with 70 sccm flow. (✗: no Fe detection; ✓: Fe detection) (b) EDX spectrum of as-deposited 15 nm film prepared from $[Fe(Cp)_2]$ and ozone at T=250 °C.

Fe_2O_3 films from $[Fe(^ipki)_2]$

Scheme of the parameters investigated to optimize the deposition of Fe_2O_3 from $[Fe(^ipki)_2]$ at $T_{Fe\text{-}subl}$= 100 °C using ozone and water as co-reactant under pressure boost or flow mode at deposition temperature window of 150-250 °C is shown in Figure S5(a). No iron was detected in the films for these conditions. Therefore, sublimation temperature was increased to 130 °C, Figure S5(b). EDX spectrum shows the presence of Fe in the deposited films performed at 250 °C with ozone, heating the iron precursor at 130 °C, Figure S5(c).

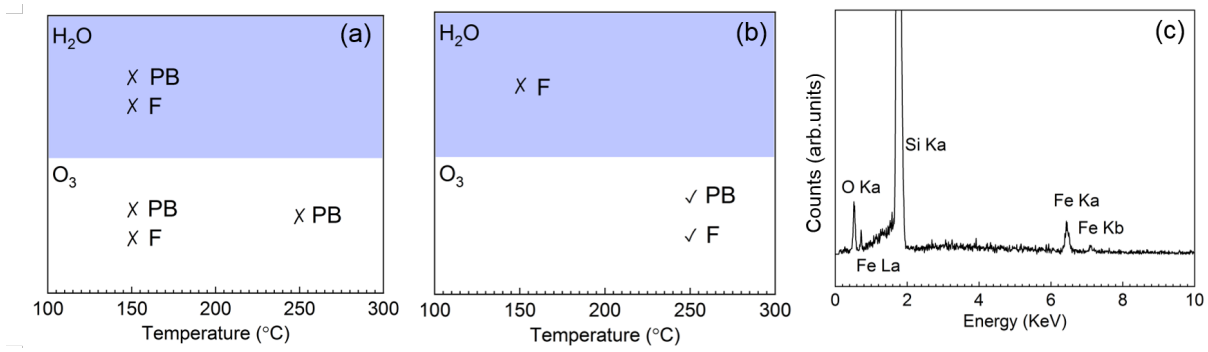

Figure S5: Optimization of Fe_2O_3 deposition from $[Fe(^ipki)_2]$ and H_2O/O_3 at sublimation temperature at (a) 100 °C and (b) 130 °C; PB is under pressure boost mode while F means using flow mode. The processes were carried out with precursor sublimation temperature at 100 °C under 70 sccm flow with 2000 cycles. (✗: no Fe detection; ✓: Fe detection). (c) Exemplary EDX spectra of the deposited Fe_2O_3 films.

Gd-Fe-O from $[Gd(DPDMG)_3]$ and $[Fe(Cp)_2]$

The AFM topographyic images obtained from both systems show homogeneous and smooth surfaces with surface roughness of $\sim$ 1 nm $\pm$ 0.1 nm, and grain size of 50 nm for the $[Gd(DPDMG)_3]$ and $[Fe(Cp)_2]$ combination and 70 nm for $[Gd(DPDMG)_3]$ and $[Fe(ipki)_2]$. Height profile is identified as black line in the topographic image and depicted at the bottom of the figure.

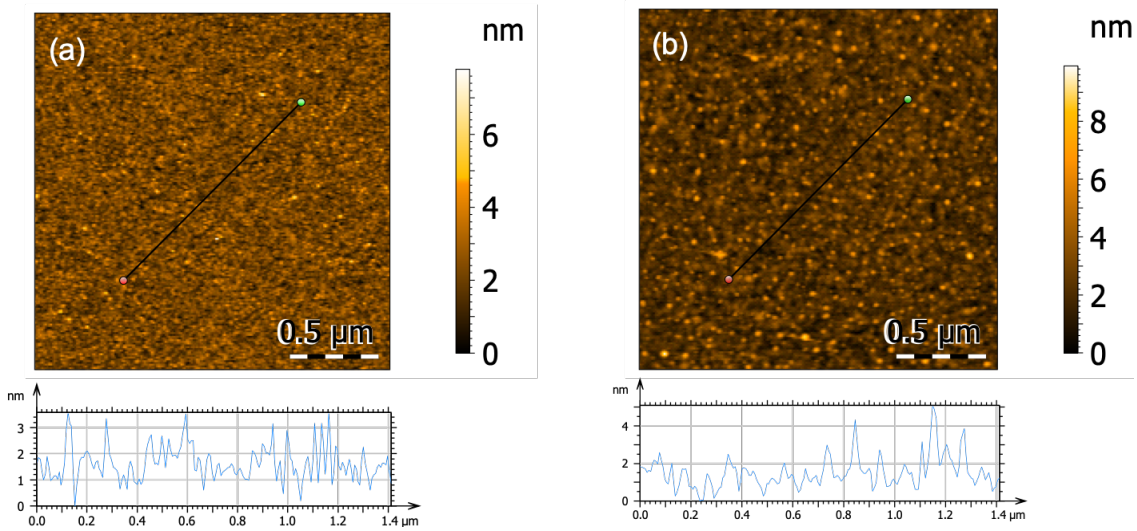

Figure S6: AFM topographic images of the $Gd_xFe_yO_z$ system obtained from (a) [Gd(DPDMG)$_3$] and [Fe(Cp)$_2$] (b) [Gd(DPDMG)$_3$] and [Fe(ipki)$_2$]. Bottom images show the height profile extracted for the respective topographic images.

XPS survey spectrum of a 30 nm $Gd_3Fe_5O_{12}$ sample combining [Gd(DPDMG)$_3$] and [Fe(Cp)$_2$] reveals the existence of Gd, Fe, O, C and Si, Figure S7. The absence of the N *1s* peaks at $\sim$ 400 eV indicates the decomposition of nitrogen containing DPDMG ligand. The quantitative ratio of Gd and Fe in the $Gd_3Fe_5O_{12}$ film was extracted from the survey spectrum taking into consideration the relative sensitivity factors (RSF) for each element.[31] The cation ratio Gd/Fe is found to be 1.77 which is very close to the theoretical value 1.67 calculated from the chemical formula of $Gd_3Fe_5O_{12}$.

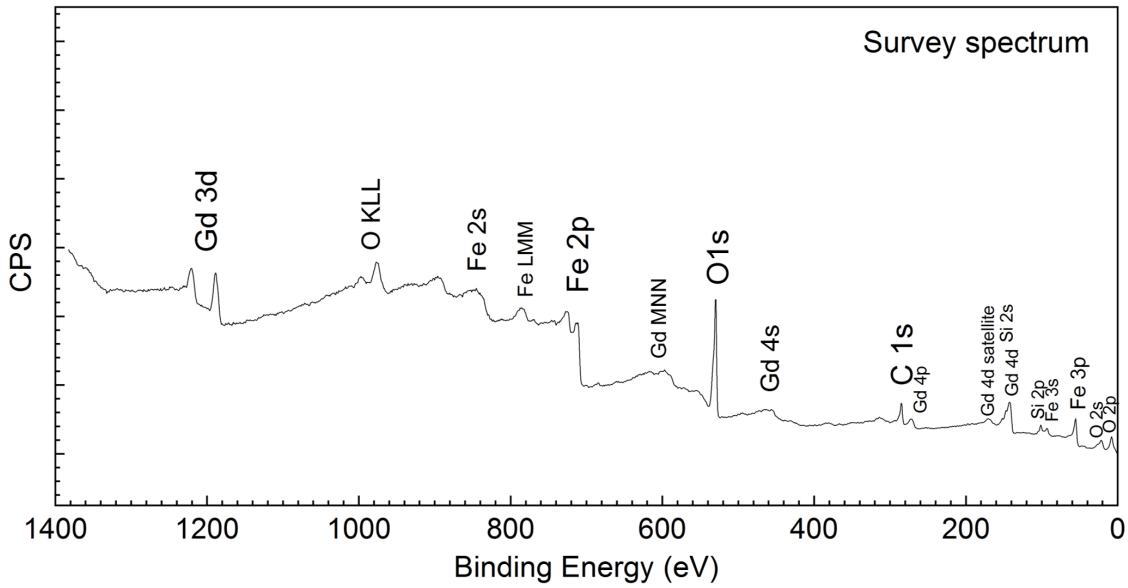

Figure S7: XPS survey spectrum of a 30 nm thick $Gd_3Fe_5O_{12}$ film annealed at 800°C for 30 min in oxygen.

Reported binding energy values for of Gd $3d$ and Fe $2p$ core level spectra in $Gd_3Fe_5O_{12}$, Gd_2O_3 and Fe_2O_3 are summarized in Table S4 and compared with our data.

Table S4: The binding energy positions of Gd $3d$ and Fe $2p$ core level spectra in $Gd_3Fe_5O_{12}$, Gd_2O_3 or Fe_2O_3 samples

	Gd $3d_{3/2}$ (eV)	Gd $3d_{5/2}$ (eV)	Fe $2p_{1/2}$ (eV)	Fe $2p_{3/2}$ (eV)	$\Delta E_{(\text{Satellite-Fe}2p_{3/2})}$ (eV)	Ref.
$Gd_3Fe_5O_{12}$ thin films	1221.1	1189.1	725.0	711.4	7.8	This work
$Gd_3Fe_5O_{12}$ films	-	1186.5	-	710.5	-	[32]
Gd_2O_3 thin films	1219.4	1187.0	-	-	-	[33]
Gd_2O_3 powder	1219.6	1187.6	-	-	-	[34]
Gd_2O_3 powder	-	1187.5	-	-	-	[35]
Gd_2O_3 nanocrystal	1220.4	1187.9	-	-	-	[36]
Fe_2O_3 films	-	-	724.3	711.2	-	[37]
Fe_2O_3 films	-	-	724.5	710.9	-	[18]
Fe_2O_3 powder	-	-	-	711.2	7.8	[38]
$\alpha-Fe_2O_3$ powder	-	-	-	710.8	8.5	[39]
$\gamma-Fe_2O_3$ powder	-	-	-	711.0	8.3	[39]

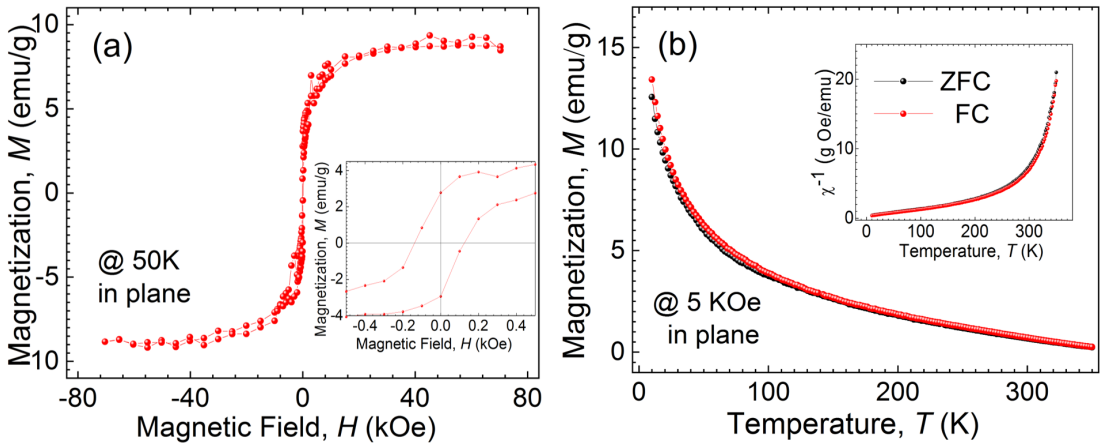

Figure S8: In plane magnetic measurements of a 30 nm thick $Gd_3Fe_5O_{12}$ sample annealed at 800°C for 30 min in oxygen: (a) field-independent magnetic hysteresis loop (M-H) at 50 K (zoom-in spectra see inset panel); (b) temperature-dependent magnetization curve (M-T) under ZFC-FC conditions at 5 KOe. Inset in (b) shows the derived reversed susceptibility under the same conditions.

Gd-Fe-O from $[Gd(DPDMG)_3]$ and $[Fe(^i pki)_2]$

The EDX spectra of samples located at different places along the gas flow path in the chamber are illustrated in Figure S9 (from **e** to **h** moving from gas inlet toward outlet). At position **e** the well-defined peaks of Gd and Fe are observed; moving to the gas outlet the films become Fe rich. This observation is also true when the Gd_2O_3, Fe_2O_3 subcycles are reversed.

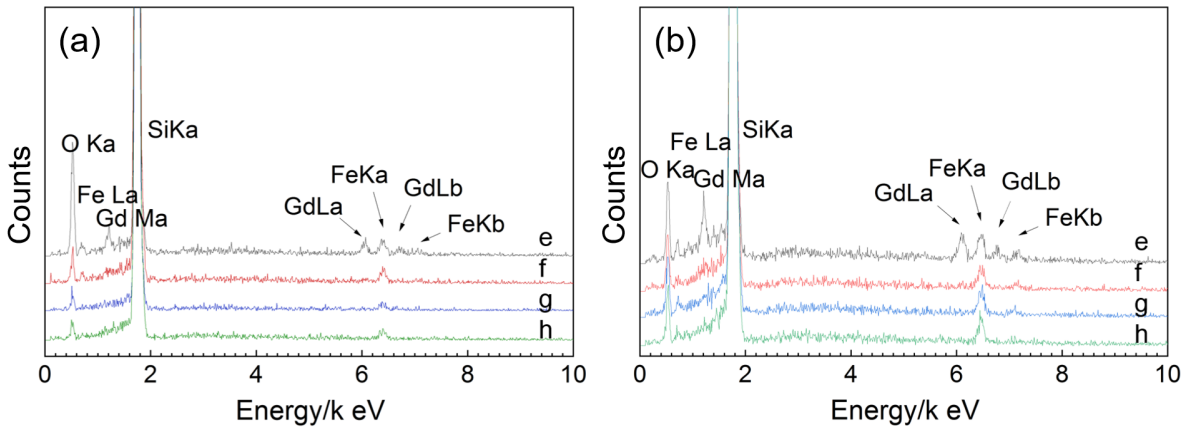

Figure S9: EDX spectra of Gd-Fe-O samples from 2Gd: 1Fe and 1Fe: 2Gd deposition process combining [Gd(DPDMG)$_3$] and [Fe(^{i}pki)$_2$] that are located at different places along the gas flow path in the reaction chamber (corresponding to the marks in Figure 10 main manuscript).

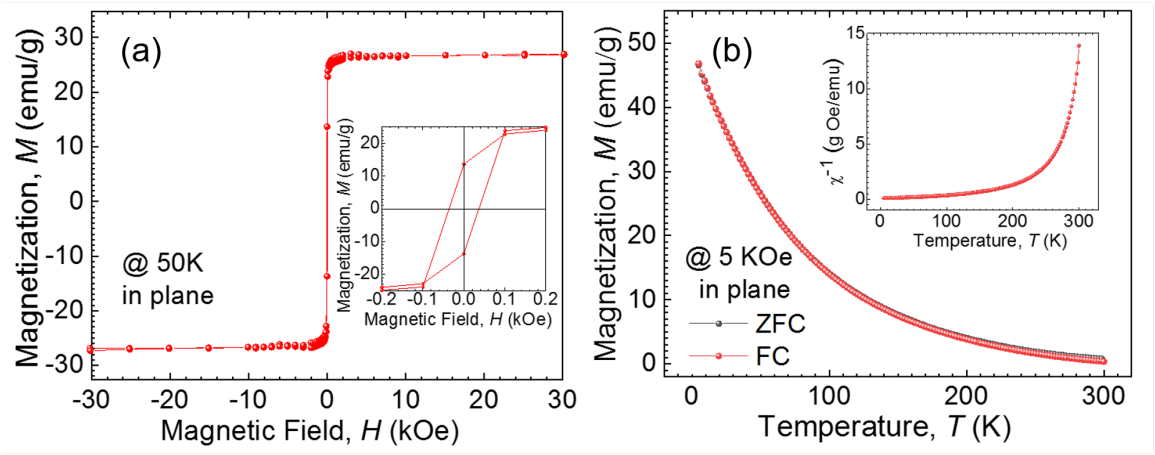

Figure S10: In plane magnetic measurements of a 120 nm thick $Gd_xFe_yO_z$ sample prepared from [Gd(DPDMG)$_3$] and [Fe(^{i}pki)$_2$] annealed at 800°C for 30 min in oxygen: (a) field-independent magnetic hysteresis loop (M-H) at 50 K (zoom-in spectra see inset panel); (b) temperature-dependent magnetization curve (M-T) under ZFC-FC conditions at 5 KOe. Inset in (b) shows the derived reversed susceptibility under the same conditions.

References

(1) Rooth, M.; Johansson, A.; Kukli, K.; Aarik, J.; Boman, M.; Hårsta, A. Atomic Layer Deposition of Iron Oxide Thin Films and Nanotubes using Ferrocene and Oxygen as Precursors. *Chemical Vapor Deposition* **2008**, *14*, 67–70.

(2) Scheffe, J. R.; Francés, A.; King, D. M.; Liang, X.; Branch, B. A.; Cavanagh, A. S.; George, S. M.; Weimer, A. W. Atomic layer deposition of iron(III) oxide on zirconia nanoparticles in a fluidized bed reactor using ferrocene and oxygen. *Thin Solid Films* **2009**, *517*, 1874–1879.

(3) Klahr, B. M.; Martinson, A. B.; Hamann, T. W. Photoelectrochemical investigation of ultrathin film iron oxide solar cells prepared by atomic layer deposition. *Langmuir* **2011**, *27*, 461–8.

(4) Li, X.; Fan, N. C.; Fan, H. J. A Micro-pulse Process of Atomic Layer Deposition of Iron Oxide Using Ferrocene and Ozone Precursors and Ti-Doping. *Chemical Vapor Deposition* **2013**, *19*, 104–110.

(5) Avila, J. R.; Kim, D. W.; Rimoldi, M.; Farha, O. K.; Hupp, J. T. Fabrication of thin films of α-Fe_2O_3 via atomic layer deposition using iron bisamidinate and water under mild growth conditions. *ACS Appl. Mater. Interfaces* **2015**, 16138−16142.

(6) de Ridder, M.; van de Ven, P. C.; van Welzenis, R. G.; Brongersma, H. H.; Helfensteyn, S.; Creemers, C.; Van Der Voort, P.; Baltes, M.; Mathieu, M.; Vansant, E. F. Growth of Iron Oxide on Yttria-Stabilized Zirconia by Atomic Layer Deposition. *The Journal of Physical Chemistry B* **2002**, *106*, 13146–13153.

(7) Nilsen, O.; Lie, M.; Foss, S.; Fjellvåg, H.; Kjekshus, A. Effect of magnetic field on the growth of α-Fe_2O_3 thin films by atomic layer deposition. *Applied Surface Science* **2004**, *227*, 40–47.

(8) Lie, M.; Fjellvåg, H.; Kjekshus, A. Growth of Fe_2O_3 thin films by atomic layer deposition. *Thin Solid Films* **2005**, *488*, 74–81.

(9) Bachmann, J.; Jing,; Knez, M.; Barth, S.; Shen, H.; Mathur, S.; Gösele, U.; Nielsch, K. Ordered Iron Oxide Nanotube Arrays of Controlled Geometry and Tunable Magnetism

by Atomic Layer Deposition. *Journal of the American Chemical Society* **2007**, *129*, 9554–9555.

(10) Lin, Y.; Zhou, S.; Sheehan, S. W.; Wang, D. Nanonet-Based Hematite Heteronanostructures for Efficient Solar Water Splitting. *Journal of the American Chemical Society* **2011**, *133*, 2398–2401.

(11) Aronniemi, M.; Saino, J.; Lahtinen, J. Characterization and gas-sensing behavior of an iron oxide thin film prepared by atomic layer deposition. *Thin Solid Films* **2008**, *516*, 6110–6115.

(12) Klug, J. A.; Becker, N. G.; Riha, S. C.; Martinson, A. B. F.; Elam, J. W.; Pellin, M. J.; Proslier, T. Low temperature atomic layer deposition of highly photoactive hematite using iron(iii) chloride and water. *Journal of Materials Chemistry A* **2013**, *1*, 11607–11613.

(13) Tanskanen, A.; Mustonen, O.; Karppinen, M. Simple ALD process for ϵ-Fe_2O_3 thin films. *APL Materials* **2017**, *5*, 056104.

(14) Escrig, J.; Bachmann, J.; Jing, J.; Daub, M.; Altbir, D.; Nielsch, K. Crossover between two different magnetization reversal modes in arrays of iron oxide nanotubes. *Physical Review B* **2008**, *77*, 214421.

(15) Martinson, A. B. F.; DeVries, M. J.; Libera, J. A.; Christensen, S. T.; Hupp, J. T.; Pellin, M. J.; Elam, J. W. Atomic Layer Deposition of Fe_2O_3 Using Ferrocene and Ozone. *The Journal of Physical Chemistry C* **2011**, *115*, 4333–4339.

(16) Riha, S. C.; Racowski, J. M.; Lanci, M. P.; Klug, J. A.; Hock, A. S.; Martinson, A. B. F. Phase Discrimination through Oxidant Selection in Low-Temperature Atomic Layer Deposition of Crystalline Iron Oxides. *Langmuir* **2013**, *29*, 3439–3445.

(17) Bratvold, J. E.; Carraro, G.; Barreca, D.; Nilsen, O. An iron(II) diketonate–diamine complex as precursor for thin film fabrication by atomic layer deposition. *Applied Surface Science* **2015**, *347*, 861–867.

(18) Peeters, D. et al. Nanostructured Fe_2O_3 Processing via Water-Assisted ALD and Low-Temperature CVD from a Versatile Iron Ketoiminate Precursor. *Advanced Materials Interfaces* **2017**, *4*, 1700155.

(19) Devi, A. 'Old Chemistries' for new applications: Perspectives for development of precursors for MOCVD and ALD applications. *Coordination Chemistry Reviews* **2013**, *257*, 3332–3384.

(20) Milanov, A. P.; Xu, K.; Laha, A.; Bugiel, E.; Ranjith, R.; Schwendt, D.; Osten, H. J.; Parala, H.; Fischer, R. A.; Devi, A. Growth of Crystalline Fe_2O_3 Thin Films with a High-Quality Interface on Si(100) by Low-Temperature H_2O-Assisted Atomic Layer Deposition. *Journal of the American Chemical Society* **2010**, *132*, 36–37.

(21) Jones, A. C.; Aspinall, H. C.; Chalker, P. R.; Potter, R. J.; Kukli, K.; Rahtu, A.; Ritala, M.; Leskelä, M. Recent developments in the MOCVD and ALD of rare earth oxides and silicates. *Materials Science and Engineering: B* **2005**, *118*, 97–104.

(22) Päiväsaari, J.; Putkonen, M.; Niinistö, L. A comparative study on lanthanide oxide thin films grown by atomic layer deposition. *Thin Solid Films* **2005**, *472*, 275 – 281.

(23) Niinistö, J.; Petrova, N.; Putkonen, M.; Niinistö, L.; Arstila, K.; Sajavaara, T. Gadolinium oxide thin films by atomic layer deposition. *Journal of Crystal Growth* **2005**, *285*, 191 – 200.

(24) Potter, R.; Chalker, P.; Manning, T.; Aspinall, H.; Loo, Y.; Jones, A.; Smith, L.; Critchlow, G.; Schumacher, M. Deposition of HfO_2, Fe_2O_3 and PrO_x by Liquid Injection ALD Techniques. *Chemical Vapor Deposition* **2005**, *11*, 159–169.

(25) Kukli, K.; Hatanpää, T.; Ritala, M.; Leskelä, M. Atomic Layer Deposition of Gadolinium Oxide Films. *Chemical Vapor Deposition* **2007**, *13*, 546–552.

(26) Vitale, S. A.; Wyatt, P. W.; Hodson, C. J. Plasma-enhanced atomic layer deposition and etching of high-k gadolinium oxide. *J. Vac. Sci. Technol. A* **2012**, *30*, 1–130.

(27) Han, J. H.; Nyns, L.; Delabie, A.; Franquet, A.; Van Elshocht, S.; Adelmann, C. Reaction Chemistry during the Atomic Layer Deposition of Sc_2O_3 and Gd_2O_3 from $Sc(MeCp)_3$, $Gd^iPrCp)_3$, and H_2O. *Chemistry of Materials* **2014**, *26*, 1404–1412.

(28) Han, J. H.; Delabie, A.; Franquet, A.; Conard, T.; Van Elshocht, S.; Adelmann, C. Ozone-Based Atomic Layer Deposition of Gd_2O_3 from Tris(isopropylcyclopentadienyl)gadolinium: Growth Characteristics and Surface Chemistry. *Chemical Vapor Deposition* **2015**, *21*, 352–359.

(29) Seppälä, S.; Niinistö, J.; Mattinen, M.; Mizohata, K.; Räisänen, J.; Noh, W.; Ritala, M.; Leskelä, M. Atomic layer deposition of lanthanum oxide with heteroleptic cyclopentadienyl-amidinate lanthanum precursor - Effect of the oxygen source on the film growth and properties. *Thin Solid Films* **2018**, *660*, 199–206.

(30) Savannah 100 & 200 Atomic Layer Deposition System User Manual. Cambridge NanoTech Inc. 2007.

(31) NIST X-ray Photoelectron Spectroscopy (XPS) Database. `https://srdata.nist.gov/xps/`.

(32) Söderlind, F.; Selegård, L.; Nordblad, P.; Uvdal, K.; Käll, P.-O. Sol–gel synthesis and characterization of polycrystalline $GdFeO_3$ and $Gd_3Fe_5O_{12}$ thin films. *Journal of Sol-Gel Science and Technology* **2009**, *49*, 253–259.

(33) Milanov, A. P. MOCVD and ALD of rare earth containing multifunctional materials: from precursor chemistry tot hin film deposition and applications. Thesis, 2010.

(34) Raiser, D.; Deville, J. Study of XPS photoemission of some gadolinium compounds. *Journal of Electron Spectroscopy and Related Phenomena* **1991**, *57*, 91 – 97.

(35) Uwamino, Y.; Ishizuka, T.; Yamatera, H. X-ray photoelectron spectroscopy of rare-earth compounds. *Journal of Electron Spectroscopy and Related Phenomena* **1984**, *34*, 67 – 78.

(36) Söderlind, F.; Pedersen, H.; Petoral, R. M.; Käll, P.-O.; Uvdal, K. Synthesis and characterisation of Fe_2O_3 nanocrystals functionalised by organic acids. *Journal of Colloid and Interface Science* **2005**, *288*, 140 – 148.

(37) Graat, P. C. J.; Somers, M. A. J. Simultaneous determination of composition and thickness of thin iron-oxide films from XPS Fe 2p spectra. *Applied Surface Science* **1996**, *100-101*, 36–40.

(38) Paparazzo, E. XPS analysis of iron aluminum oxide systems. *Applied Surface Science* **1986**, *25*, 1–12.

(39) Grosvenor, A. P.; Kobe, B. A.; Biesinger, M. C.; McIntyre, N. S. Investigation of multiplet splitting of Fe 2p XPS spectra and bonding in iron compounds. *Surface and Interface Analysis* **2004**, *36*, 1564–1574.

Table of contents